Check for updates

ADVANCED QUANTUM TECHNOLOGIES
www.advquantumtech.com

Versatile Quadrature Antenna for Precise Control of Large Electron Spin Ensembles in Diamond

Ruben Pellicer-Guridi, Koen Custers, Joseba Solozabal-Aldalur, Alexey Brodolin, Jason T. Francis, Miguel Varga, Asier Mongelos, Jorge Casanova, Margarethus M. Paulides, and Gabriel Molina-Terriza*

An easily reproducible inexpensive microwave antenna that can generate a strong and homogeneous magnetic field of arbitrary polarization is presented, which enables fast and coherent control of electron spins over a large volume. Unlike preceding works, a resonant antenna with ample optical access and which maintains its resonant behavior regardless of the proximity of other experimental hardware components is presented. This robustness is crucial as it enables using microscope objectives with short working distances to perform wide-field imaging/sensing with bulk diamonds. The antenna generates a magnetic field strength of 22.3 A m^{-1} for 1 W total driving power, which doubles the power efficiency compared with previously reported patch antenna designs. The magnetic field homogeneity in a volume of 0.3mm^3, 0.6mm^3 and 1mm^3 is within 3%, 8% and 14%, respectively. The antenna can be driven off-resonance without affecting the ellipticity and inhomogeneity of the field, and has a full-width-at-half-maximum bandwidth of ∼200 MHz. Its resonant frequency can be tuned over a 400 MHz range via varactors. The PCB files are provided open-source. This work facilitates a robust and versatile piece of instrumentation, being particularly appealing for applications such as high sensitivity magnetometry and wide-field imaging/sensing with nitrogen-vacancy centers.

1. Introduction

Nitrogen-Vacancy (NV) centers in diamond have emerged as a promising platform for quantum sensing due to their exceptional properties, such as long coherence times even at room temperature, high sensitivity, and nanoscale spatial resolution. They have been used to detect various physical quantities, including magnetic and electric fields, temperature, and strain.[1] Furthermore, their robustness, wide working temperature range and optical addressability make them attractive candidates for practical applications in diverse fields such as materials science, biomedicine, and fundamental physics.[1–3]

The negatively charged (NV^-) conformation is the most explored configuration due to its remarkable optical and spin properties,[4] and will be referred to as NV during the rest of this manuscript. In this configuration, a valence electron and an extra electron form a spin pair $S = 1$ that holds a spin triplet with state $m_s = 0, +1$

R. Pellicer-Guridi, J. Solozabal-Aldalur, J. T. Francis, M. Varga, A. Mongelos, G. Molina-Terriza
Centro Física de Materiales
Donostia-San Sebastián 20018, Spain
E-mail: ruben.pellicer@ehu.eus

R. Pellicer-Guridi, A. Brodolin
Donostia International Physics Center
Donostia-San Sebastián 20018, Spain

K. Custers
Medical Image Analysis
Dept. Biomedical Engineering
Eindhoven University of Technology
Eindhoven 5612, Netherlands

K. Custers, M. M. Paulides
Care&Cure Lab of the Electromagnetics Group (EM4Care+Cure)
Dept. Electrical Engineering
Eindhoven University of Technology
Eindhoven 5600, The Netherlands

J. Casanova
EHU Quantum Center
Univeristy of the Basque Country UPV/EHU
Leioa 48940, Spain

J. Casanova
Department of Physical Chemistry
University of Basque Country UPV/EHU
Bilbao 48080, Spain

M. M. Paulides
Dept. Radiotherapy, Cancer Institute
Erasmus University Medical Center
Rotterdam 3015, The Netherlands

G. Molina-Terriza
IKERBASQUE
Basque Foundation for Science
Bilbao 48009, Spain

The ORCID identification number(s) for the author(s) of this article can be found under https://doi.org/10.1002/qute.202400142

© 2024 The Author(s). Advanced Quantum Technologies published by Wiley-VCH GmbH. This is an open access article under the terms of the Creative Commons Attribution-NonCommercial License, which permits use, distribution and reproduction in any medium, provided the original work is properly cited and is not used for commercial purposes.

DOI: 10.1002/qute.202400142

25119044, 2025, 3, Downloaded from https://advanced.onlinelibrary.wiley.com/doi/10.1002/qute.202400142 by Universidad del Pais Vasco Biblioteca Universitaria, Wiley Online Library on [02/04/2025]. See the Terms and Conditions (https://onlinelibrary.wiley.com/terms-and-conditions) on Wiley Online Library for rules of use; OA articles are governed by the applicable Creative Commons License

or −1. Initialization and readout of the spin state are commonly done with a green laser and spin control is achieved via microwave (MW) fields.[5] This control is enabled by the Zeeman effect by which the $m_s = \pm 1$ spin states are energetically separated in the presence of an external magnetic field. This energy gap between the electron spin states enables the manipulation of spin states into an arbitrary superposition with $m_s = 0, +1$ and −1 by means of MW fields. The energy gap between the three electron spin states depends on the external magnetic field following the simplified electron spin Hamiltonian

$$H = DS_z^2 - \gamma_e \vec{B} \cdot \hat{S} \quad (1)$$

where $D = 2.87$ GHz is the zero-field splitting parameter, $\hat{S}$ is the vector of spin operators and $\gamma_e = 2.8$ MHz G^{-1} is the gyromagnetic ratio of the electron.[6]

Working near the degeneracy conditions of the $m_s = \pm 1$ states, e.g., without an externally provided bias magnetic field,[7] hinders spin control as linearly polarized MW fields cannot address the $m_s = \pm 1$ states individually without introducing strong constraints in pulse sequences.[8] Conversely, circularly polarized MW fields can act selectively on $m_s = +1$ or $m_s = -1$ states depending on the direction of the polarization.[9]

In this context, the design and the characteristics of the MW antenna used for NV center experiments play a crucial role in achieving efficient and precise manipulation of the NV center's spin states. Besides generating a strong magnetic field, providing a MW antenna with the capability of generating highly homogeneous fields and arbitrary polarization greatly enhances its potential. The homogeneity is crucial as large ensembles of NV centers can be advantageous for several applications, i.e., vector magnetometry determining both direction and magnitude of magnetic fields simultaneously,[10] parallel sensing in different spatial locations for imaging applications,[11] improving measurement sensitivity by averaging the responses of multiple NV centers,[12] NMR spectroscopy with NV ensembles,[13] etc.

When employing single NV centers it is a common practice to use a simple straight wire or a loop to generate the MW fields, but these antennas are not suitable to control NV ensembles as their fields possess large spatial variations. Furthermore, it is more difficult to achieve orthogonality between the MW magnetic field and that of the external static one at the location of the NV center.[14,15] Whilst several MW antennas have been proposed to address these homogeneity limitations, most are limited to generating linearly polarized fields.[16–20]

Regarding the arbitrary polarization capability, this is particularly appealing as it can selectively deactivate interactions from the −1 or the +1 spin populations via applying a clockwise or an anti-clockwise circularly polarized field. Several approaches have been proposed that are capable of generating circularly polarized MW magnetic fields but with reduced field homogeneity. A pair of wires aligned either orthogonally or perpendicularly has been used to generate circularly polarized magnetic fields. Such designs based on thin straight wires are placed a few µm away from the NV centers to achieve high magnetic field ratios and suffer very high spatial inhomogeneity.[21,22] Wide bandwidth microstrip resonators have been proposed on standard PCBs[23] and on optically transparent conductive materials,[24] with the former blocking the optical access from one face of the diamond and the latter enhancing this access at the expense of requiring non-standard manufacturing processes and materials. These microstrip designs improve the homogeneity in the plane parallel to the surface. However, they still present large field variations along the direction orthogonal to the microstrip, constraining the effective volume homogeneity.[24]

Having a MW antenna capable of generating strong and homogeneous circularly polarized fields remains being a challenge. Resonant antennas can offer a solution to covering a large volume with a strong and homogeneous field.[25,26] Yet, the designs proposed to date have important limitations that severely hinder their applicability such as their resonant behavior being heavily affected by components in their proximity, which is indispensable for the antenna to work reliably.[19,25] A dielectric ceramic resonator with tailored high dielectric constant has been proposed, which achieves a Rabi frequency of 3.9 MHz $W^{-1/2}$, and a full width at half maximum bandwidth (FWHM) of 140 MHz at 2.67 GHz (estimated from the S-parameters), and an excellent theoretical inhomogeneity of 4% (reported as standard deviation) over a cylindrical volume of 5.9 mm^3 (measured ∼ 7.3% over 0.45 mm^3).[26] Unfortunately, this design is limited by design to a fixed resonant frequency. Moreover, this ceramic resonator is non-trivial to reproduce as it relies on being able to manufacture on a special substrate, which is out of the reach of most labs. Additionally, its homogeneity volume is more than 2.5 mm away from the optical access faces restricting its use to specialty microscope objectives with ultra-long working distance.

A planar design was proposed with very appealing properties such as an actively re-tunable resonant frequency and seamless reproducibility with standard PCB materials and manufacturing processes.[25] This previous reference work featured 165 MHz FWHM (estimated from the S-parameters) and enabled a Rabi frequency of 0.8 MHz $(\sqrt{W})^{-1}$.[25] However, this design shows a strong shift in the resonant frequency of ∼70 MHz due to the position of an objective lens, only offers optical access from one side, and has considerably worse inhomogeneity. To the best of our knowledge, no resonant MW antenna capable of generating circular polarization has been reported that is robust against external hardware components commonly employed with NV center setups. Furthermore, none of the above works analyze important features such as the field strength when working off-resonance and the ellipticity over the volume of interest, which are crucial for their usability.

Here we present an efficient quadrature MW antenna that maintains its calibrated resonant behavior regardless of the configuration of its neighboring setup components. This largely reduces setup constraints otherwise introduced by antennas whose behaviour is dependent on nearby elements,[25] and enables dynamic configurations such as scanning movements of microscope objectives. Furthermore, the design proposed here complements the benefits of the design of Herrmann et al.[25] with enhanced optical access, power efficiency, and reproducibility. The antenna has been tested numerically and experimentally to validate its reflection and transmission coefficients, magnetic field amplitude and homogeneity, and power dissipation. Moreover, we show that the S-parameter curves are not a precise indicator of how the magnetic field strength changes with frequency. Similarly, unlike preceding works, we also analyze the ellipticity and inhomogeneity of the field over a volume of interest in

 © 2024 The Author(s). Advanced Quantum Technologies published by Wiley-VCH GmbH

off-resonance conditions, and show that this design maintains fine response over large volumes of NVs even at frequencies far from resonance. Being aware that MW antennas are one of the few elements not available off-the-shelf, we offer open-source the files required to reproduce the antenna and accelerate scientific progress and reproducibility.[27] Thereby, given its performance, versatility, robustness and accessibility, this antenna can be the go-to solution for many NV setups in many labs.

2. Design Materials and Methods

2.1. Antenna Design

The antenna has been designed to generate strong and homogeneous circularly polarized fields while providing ample optical and mechanical access and fabrication simplicity. The planar geometry of the circular patch antenna together with the through hole to host the diamond facilitates easy access space on both sides of the PCB so other setup components, like microscope objectives with short working distances or samples to be analyzed, can be brought in close proximity to the diamond. This design also offers more flexibility when designing optical path configurations because optical pumping and fluorescence collection can be performed from both faces of the diamond. The resonant frequency of the prototype is designed to be 2.86 GHz. However, to enable efficient control of the $m_s = 0 \Longleftrightarrow -1$ transition, the resonant frequency can be tuned to lower frequencies by adding capacitors to the antenna. As mentioned earlier, two important design constraints are achieving a high field strength and high homogeneity over a large volume in the diamond. Importantly, to harvest the highest signal-to-noise ratio, the location and shape of this volume should be such that it can be optically addressed in a manner that the NVs contained in the optimally controllable volume are all interrogate at once, while minimizing the fluorescence from NVs not contained in this volume.

An electromagnetic field simulation software (CST Studio Suite 2023, Dassault Systèmes, Vélizy–Villacoublay, France) is used to optimize antenna design parameters. An initial geometry is estimated from analytical expressions for circular patch antennas derived in ref. [28]. The antenna is sized to match its first resonant mode TM_{110} to the desired MW frequency. This mode induces the most homogeneous and the largest magnetic field that is achievable with this type of circular antenna.[28] Its corresponding resonant frequency is estimated by:

$$(f_r)_{110} = \frac{1.8412c}{2\pi a\sqrt{\epsilon_r}} \tag{2}$$

where c is the speed of light, a is the radius of the antenna and ϵ_r is the permittivity in the dielectric material, also called the dielectric constant. The TM_{110} mode presents the highest magnetic field at the center of the antenna. Therefore, the positioning for the diamond has to be chosen accordingly. Other higher frequency modes could be excited but these will result in a lower and less homogeneous magnetic field. The antenna is designed with a square hole, so that it can host a diamond as large as 3 x 3 x 0.5 mm^3, which covers most commercially available single crystal samples. The effect of the size of the hole on the resonant frequency is minor as long as its size remains considerably smaller than the size of the patch. The size of the hole can be tailored to trade field homogeneity by field strength; a larger hole creates a more homogeneous field at the expense of reducing the field strength.

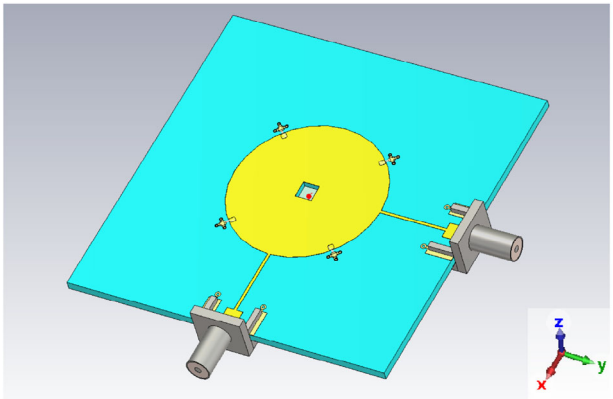

Figure 1. Simulated antenna for MW excitation of the NV center. It consists of a circular patch with two feeding ports. The PCB is double-sided with a bottom copper plane covering the whole PCB area, excluding a centered square through hole that contains an embedded bulk diamond.

The simulations also include the diamond material with the aforementioned size, a dielectric constant ϵ_r of 5.7, and placed in the center of the hole. For an antenna resonant at 2.86 GHz, the outer diameter of the patch is a = 14.12 mm, the quarter wavelength transmission line is 12,46 mm long and 0.53 mm wide, the copper thickness is 0.035 mm, and the FR4 is 1.55 mm thick. A quarter wavelength transmission line is used to match the impedance of the circular patch antenna to the 50 Ω of the transmission chain. This enables efficient power transfer and high signal integrity. The feeding ports are connected to the outer edges of the circular patch, allowing surface currents to run through the patch without disturbance. This configuration ensures that the strongest magnetic field is created in the middle of the patch.

Due to its common availability, we have chosen FR-4 as PCB substrate, which has an ϵ_r of 4.4. According to Equation (2), by changing the dielectric constant, the size of the patch of the antenna will change proportionally with the factor of $\sqrt{\epsilon_r}$. Reducing substrate thickness also increases the magnetic field, but considerably penalizes the homogeneity along the Z direction. Coaxial 50 Ω SMA connectors are used for signal launch to the PCB, minimizing power reflections and providing a robust and reproducible performance. The antenna is visualized in **Figure 1**.

2.2. Simulation Results

In **Figure 2** and Figure S1 (Supporting Information) we present the simulations performed under different input polarization conditions. According to the simulations shown in Figure 2, for the circular polarization mode, the inhomogeneity is within 14% in a 1 mm^3 cylinder (500 µm height and 800 µm radius). For smaller volumes of 0.6 mm^3 and 0.3 mm^3, the inhomogeneity is within 8% and 3% respectively. In linear polarization modes (see Figure S1, Supporting Information) the inhomogeneity is lower in the xy plane direction orthogonal to the axis of the feeding port, e.g., in the figure the feeding port is along the x = 0 axis, leading

© 2024 The Author(s). Advanced Quantum Technologies published by Wiley-VCH GmbH

25119044, 2025, 3, Downloaded from https://advanced.onlinelibrary.wiley.com/doi/10.1002/qute.202400142 by Universidad del Pais Vasco Biblioteca Universitaria, Wiley Online Library on [02/04/2025]. See the Terms and Conditions (https://onlinelibrary.wiley.com/terms-and-conditions) on Wiley Online Library for rules of use; OA articles are governed by the applicable Creative Commons License

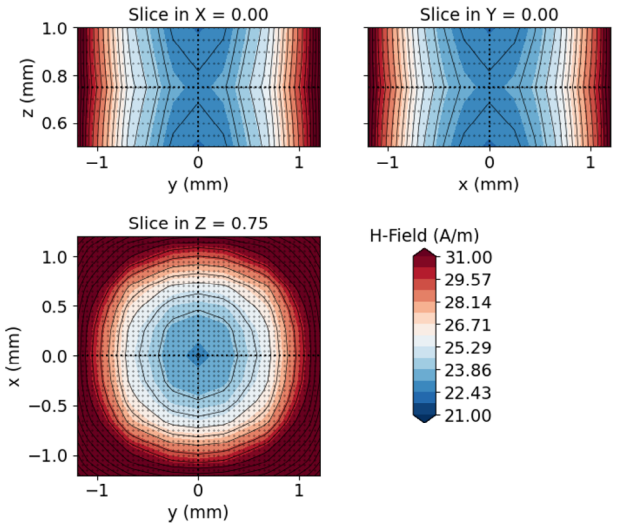

Figure 2. Simulated H-field for circular polarization mode. Cross-sections of the H-field on x, y, and z planes in the middle of the diamond. The values correspond to RMS values for 0.5 W per port fed with a 90° dephase between them.

the y = 0 axis to have lower inhomogeneity. The field strength is most homogeneous near the center of the diamond in the xy plane, which also holds a local minimum for this plane. In the z axis, the field is the strongest and most homogeneous around the center of the PCB depth. We found no significant difference in field strength and homogeneity between having a round or a square central hole.

The spatial distribution of the magnetic field strength along the X and Y dimensions is elliptical, as can be seen in Figure S1 (Supporting Information). This ellipticity is similar on both ports but rotated by 90° according to the spatial location of each port. The combination of the contribution of both ports generates a more circular RMS magnetic field as shown in Figure 2.

The RMS magnetic field values in the center of the region of interest is 22.8 A m^{-1} RMS for 1 W total driving power in both driving modes, as visualized in Figure 2 (see also Figure S1, Supporting Information, for the linearly polarized field map).

Figure 3 shows that the direction of the linearly oscillating magnetic field is parallel to the x axis when the port along the x = 0 axis is fed. Similarly, the field oscillates parallel to the y

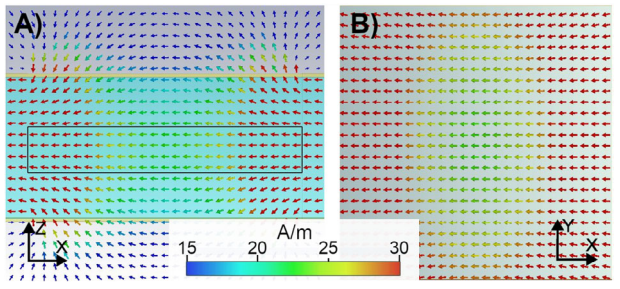

Figure 3. Arrow plot visualizing the direction of the H-field for linear polarization mode evaluated at the center of the diamond on the planes perpendicular to y (A) and z (B). The arrows show that the field is highly aligned in the x direction when driving the port along the x = 0 axis.

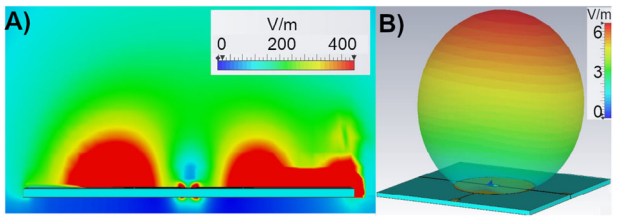

Figure 4. Plots of the E-field outside the antenna. The near field contour plot (A) and the far field plot (B) show that the external E field is mainly constrained to the top of the patch, which minimizes its coupling to external components in all other directions.

when feeding through the other port along the y = 0 axis. Combining both feds with a dephase of 90° generates the circularly polarized field.

As shown in **Figure 4**, the near and far electric fields extend almost exclusively beyond the boundaries of the body of the antenna on the side of the patch, with the ground plane acting as a shield for the other side. This largely minimizes any coupling that external elements could have with the antenna on any side other than the top of the patch. This ensures that once the response of the antenna is characterized, the user can approach the integration of the antenna on the setup without affecting its behavior. It should be noticed that the antenna is sensitive to elements on the patch side.

The H field remains within 3 dB over 192 MHz, which is significantly higher than the 120 MHz estimated from the reflection coefficient as can be seen in **Figure 5A**. In this figure, the estimation based on the S-parameters (red curve) has been derived assuming that the H-field strength is proportional to the square root of the non-reflected power, method which in this case introduces a 30% underestimation of the bandwidth (BW).

The ellipticity of the circularly polarized field is calculated by the difference between the long and the short axes of the elliptical precession of the MW vector field, and divided by the mean value of the field magnitude. **Figure 6** visualizes the contour plots of the ellipticity in percentage along the center of the hole. **Figure 7** visualizes the deviation isosurface plots for both inhomogeneity and

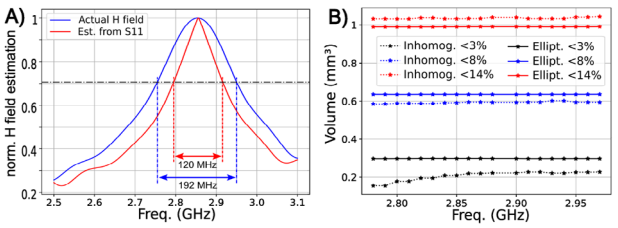

Figure 5. Plots showing the dependence of the H-field magnitude, the inhomogeneity and the ellipticity on off-resonance use with an antenna tuned to 2.86 GHz. A) Comparison between the 3dB BW for the H field calculated directly versus the widespread practice of estimating it from the S-parameters under the assumption that the H-field is proportional to the square root of the absorbed power. The latter one underestimates the BW by 30% in this case. B) Plots indicating the volume within a contained deviation of inhomogeneity and ellipticity when driven off-resonance. The dotted and the continuous lines indicate the volume within inhomogeneity and ellipticity thresholds, respectively, for deviations smaller than 3%, 8%, and 14%.

© 2024 The Author(s). Advanced Quantum Technologies published by Wiley-VCH GmbH

25119044, 2025, 3, Downloaded from https://advanced.onlinelibrary.wiley.com/doi/10.1002/qute.202400142 by Universidad del Pais Vasco Biblioteca Universitaria, Wiley Online Library on [02/04/2025]. See the Terms and Conditions (https://onlinelibrary.wiley.com/terms-and-conditions) on Wiley Online Library for rules of use; OA articles are governed by the applicable Creative Commons License

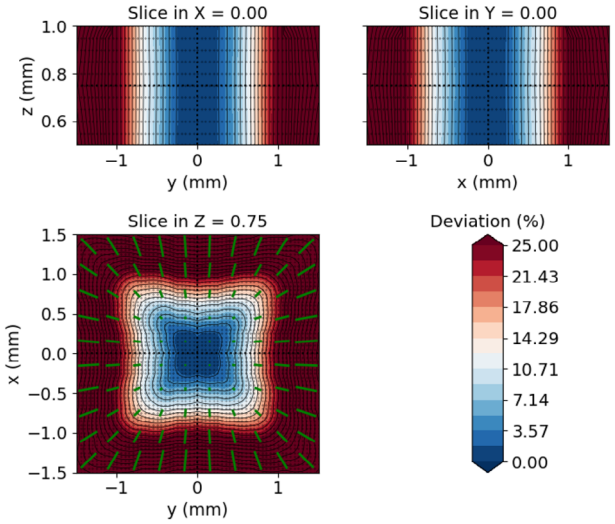

Figure 6. Simulated ellipticity map showing the spatial distribution of the deviation from circular polarization. The green lines visualize the direction of the long axis of the ellipticity and their length is proportional to the ellipticity.

ellipticity. Importantly, the low inhomogeneity and the low ellipticity contours have a large part of their volume in common, as can be inferred from Figure 7. The volume quantities are shown in Figure 5B for the deviation thresholds of 3%, 8%, and 14%. This last plot shows how the inhomogeneity and the ellipticity are affected when driving off-resonance an antenna tuned to 2.86 GHz, with only the 3% inhomogeneity volume (black dotted line) presenting substantial changes at low frequencies.

3. Experimental Validation

3.1. Antenna Fabrication and Electrical Characterization

An antenna designed to host a 3 x 3 x 0.5 mm^3 diamond size is built on a double-sided standard FR-4 PCB (Figure 9B). A commercially available diamond sample containing a high density (~4.5 ppm) of NV centers (DNV™ B14, Element Six Ltd, UK) is embedded in the hole of the MW antenna. Two high-frequency SMA PCB edge launch connectors (ref. 142-9701-811, Cinch Connectivity Solutions, USA) are soldered onto the PCB, which are non-magnetic to minimize any distortion of DC fields when performing magnetic field measurements.

To drive the antenna in a linearly polarized mode, a MW drive signal is fed through one of the ports. To generate the circularly

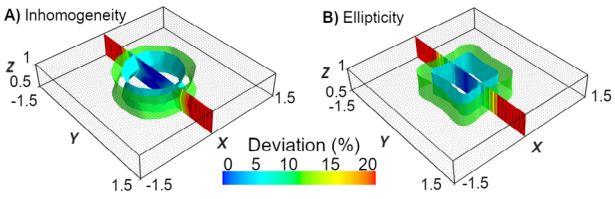

Figure 7. Isosurface plots of the inhomogeneity A) and the ellipticity B) volumes for 5% and 10% deviation. The rectangular black frames delimit the edges of the hole in the antenna.

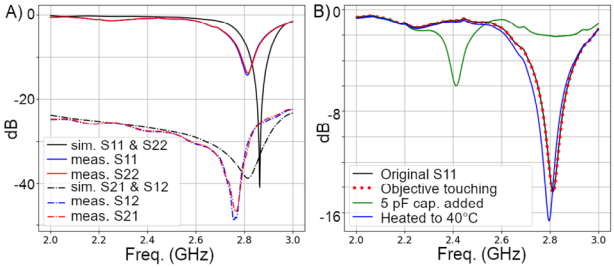

Figure 8. Plots of the measured and simulated reflection and transmission parameters of the antenna. A) Plots of the measured and simulated reflection and transmission parameters of the antenna. The resonant frequency is 55 MHz lower in the manufactured antenna (2.809 GHz) as compared with the simulations (2.864 GHz). The reflection parameters of the manufactured antenna are –14 dB as compared with the theoretical –41 dB of the simulations. The transmission parameters are below –22 dB in all cases. Both ports of the manufactured antenna show a very similar response (blue and red lines). B) Measured reflection coefficients of the antenna under different conditions. The black dotted curve shows the behaviour of the antenna under standard operation conditions. The red line shows the antenna when the microscope objective is placed against the ground plane. The overlap between the dotted black line and the red line shows no change in the resonant frequency, confirming the robustness of the antenna to external hardware components approached from the ground plane. The green line visualizes the tunability of the antenna via lumped capacitors, in this case 5 *pF*. The blue line shows the effect of temperature on the behaviour of the antenna, where a change from 22°*C* to 40°*C* decreases the resonant frequency by 16 MHz.

polarized modes, the MW drive power signal is split into two 90° phase shifted signals with a 90° phase shifting power splitter (ZX10Q-2-34-S+, Mini-circuits, NY, USA), outputs of which are connected to the two ports of the antenna. The power fed to each port is balanced in amplitude with an adjustable attenuator and calibrated in phase via an adjustable phase shifter. Right or left circularly polarized fields are generated by swapping the order of the cables at the power splitter. A vector network analyzer (Fieldfox N9912A, Keysight, USA) is used to measure the reflection (S11 and S22) and transmission (S21 and S12) coefficients of the antenna, and to calibrate the power delivered to the antenna. The results of these measurements can be observed in **Figure** 8A. Overall, the experimental and simulated S parameters agree qualitatively. However, a small shift in the expected resonant frequency of the antenna and a worsening of the reflection coefficient can be observed. The simulated and measured response time of the antenna is 2 ns, which corresponds to a quality factor of 17.6 and a Full width at half maximum (FWHM) of 120 MHz[29] and is in good agreement with the frequency response reflected in Figure 8A.

We have also tested the antenna under different conditions, to observe the resonant behaviour of the antenna (Figure 8B). For example, we have added SMD capacitors of 5 pF with case code 0603 (1608 metric) to the antenna for lowering the resonance frequency of the MW antenna from 2.81 to 2.41 GHz. This configuration reduces the resonant frequency by 400 MHz, which is equivalent to a dynamic range of almost 15 mT for the DC external magnetic field. It should be noted that the efficiency of the antenna is reduced by half when capacitively tuned to 2.41 GHz.

One important feature of this antenna is that it is very stable under changes in external conditions. For example, in Figure 8B

© 2024 The Author(s). Advanced Quantum Technologies published by Wiley-VCH GmbH

25119044, 2025, 3, Downloaded from https://advanced.onlinelibrary.wiley.com/doi/10.1002/qute.202400142 by Universidad del Pais Vasco Biblioteca Universitaria, Wiley Online Library on [02/04/2025]. See the Terms and Conditions (https://onlinelibrary.wiley.com/terms-and-conditions) on Wiley Online Library for rules of use; OA articles are governed by the applicable Creative Commons License

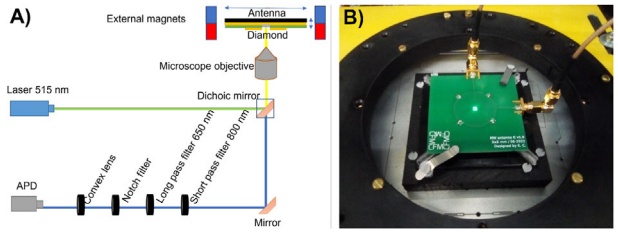

Figure 9. Simplified schematic and overview of the confocal microscope and picture of the antenna. A) Overview of the confocal microscope employed to evaluate the MW antenna, with emphasis on the optical components. Shown are the pumping path (green laser), the confocal reading path (red and yellow), the permanent magnets array and the MW antenna. B) Photograph of the MW antenna during a measurement.

it can be observed that the features of the antenna do not change at all even if the optical microscope is in contact with the antenna. Also, changes in the temperature have a small effect on the resonant behaviour of the antenna.

3.2. Setup

An optical setup is built to evaluate the manufactured MW antenna prototype. The setup allows sweeping through the volume of the diamond. The simplified schematic of the system can be found in **Figure** 9A. A green laser (iBeam-smart, 515 nm, Toptica, Germany) is used to excite the NV centers. The position of the antenna is determined by a micro-positioner that is programmatically controlled in the x, y and z-axes (X-NA08A25-E09 Zaber, Canada and SPM-MZ, Mad Citylab, Switzerland). The excitation green laser beam is focused onto the sample with a microscope objective (LU Plan ELWD 50x, NA 0.55, WD 10.1, Nikon, Japan), which also collects the fluorescence from the diamond. This fluorescence is separated from the green excitation light by a dichroic mirror, a 515 nm notch filter, a 650 nm long pass (LP) filter and an 800 nm short pass (SP) filter. The intensity of this red fluorescence is measured by an avalanche photo-diode (A-CUBE-S3000-03, Laser Components, Germany).

The MW signal is generated via a vector signal generator (SMJ100A, Rohde & Schwarz, Germany) and a power amplifier ~43 dB (ZHL-16W-43-S+, Mini-circuits, USA). A fast solid state switch (ZASWA-2-50DRA+, Mini-circuits, USA) is placed between the signal generator and the power amplifier when short pulses are needed.

3.3. External Magnetic Field

An external static magnetic field highly stable and homogeneous is generated via a ring with permanent magnets placed at a radial distance of 80 mm. This ring can host up to 32 square magnets of 12 mm length. NdFeB magnets of grade N48 are employed. This external magnetic field points along the z direction, i.e., orthogonal to the PCB of the MW antenna. The applied external magnetic field is fine-tuned for the Larmor frequency of the $m_s = 0 \Longleftrightarrow -1$ transition corresponding to $f \cong 2.81$ GHz following Equation (1).

3.4. Acquisition Sequences

An Electron Spin Resonance (ESR) experiment is performed to confirm that the $B_z \cong 2$ mT external magnetic field normal is normal to the PCB and, since the crystallographic orientation of the used diamond is 100, this field is aligned with the same angle to all NV axes (54.7°). Thereby, all the NVs will respond to the same MW frequency.

The strength and polarity of the MW field generated by the antenna are measured with a Rabi experiment on the $m_s = 0 \Longleftrightarrow -1$ electron spin transition. The sequence consists of MW pulses with different time durations. Subsequently, the oscillation frequency of the obtained photoluminescence is analyzed. The Rabi frequency is estimated by fitting the signal to an exponentially decaying oscillation according to

$$S = A\sin(2\pi\,\Omega\,\tau + \theta)\,\exp\left(-\frac{\tau}{T_2}\right) + B\tau + C \tag{3}$$

where Ω is the Rabi frequency, A is the amplitude of the signal, τ is the MW pulse duration, θ is a phase offset factor, T_2 is the decay ratio, B is a linear drift and C a DC offset.

The Rabi frequency is proportional to the MW magnetic field generated by the antenna,[26]

$$\Omega = 2\gamma_e|\langle 0|\hat{S}_x|1\rangle B| = \gamma_e\mu_0\mu_r H_{rms} \tag{4}$$

where an additional $\sqrt{2}$ is multiplied in the case of circular polarization. Also, $H_{rms} \propto \sqrt{P_{ant}}$, the square root of the input power to the antenna.

Figure 13A shows that the Rabi oscillations mediated by the antenna follow this theoretical linear dependency between the square root of the applied power and the Rabi frequency. This verifies that the antenna works in a linear regime, which is important to calibrate the MW power delivered to the diamond sample.

3.5. Experimental Characterization of Inhomogeneity

The distribution of Rabi frequencies across different planes (xy, xz, and yz) is analyzed using both circular and linear polarization. This spatial distribution is characterized by stepping the position of the antenna and the diamond with the micropositioner, sweeping the spot being interrogated in the diamond. For circular polarization, the antenna is fed with a total input power of 2.8 W calibrated and equally divided to each port; For linear polarization, 3.8 W is applied to a single port.

The resulting Rabi frequency map is illustrated in **Figure 10** (see also Figure S1 (Supporting Information) for the linearly polarized field map). A uniform sampling grid is used with 0.05 mm x 0.05 mm resolution in the xy-direction and 0.02 mm in the z-direction. The maps exhibit good agreement with the magnetic fields obtained from the simulations (see Figure 2 for the circular polarization, and also the Figure S2, Supporting Information, for the linearly polarised field map). Among the observed frequencies, the Rabi frequency recorded in the symmetry center of the contour plots is 1.86 MHz for circular polarization and 1.55 MHz for linear polarization. These Rabi frequencies correspond

© 2024 The Author(s). Advanced Quantum Technologies published by Wiley-VCH GmbH

25119044, 2025, 3, Downloaded from https://advanced.onlinelibrary.wiley.com/doi/10.1002/qute.202400142 by Universidad del Pais Vasco Biblioteca Universitaria, Wiley Online Library on [02/04/2025]. See the Terms and Conditions (https://onlinelibrary.wiley.com/terms-and-conditions) on Wiley Online Library for rules of use; OA articles are governed by the applicable Creative Commons License

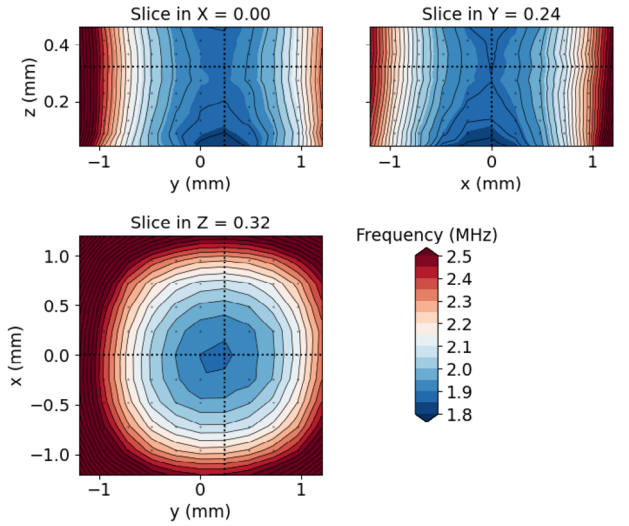

Figure 10. Measured Rabi frequency distribution maps for a circular polarized excited antenna at 2.8 W total input power. The excitation MW frequency is 2.81 GHz, corresponding to the $m_s = 0 \iff -1$ transition at an external magnetic field of $B_z \cong 2$ mT.

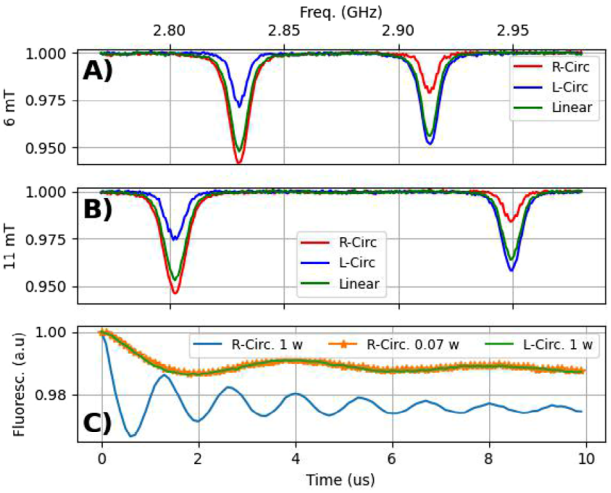

Figure 11. Measured signals showing the effect of polarization on the ESR transitions. In A) and B), the ESR signals are shown for both right and left circular polarizations for two external DC magnetic fields. The ESR for linear polarization is also shown as a reference. The measurements show that the $0 \iff 1$ ($0 \iff -1$) transition is much more power efficient with left (right) circular polarization. An example of the Rabi signals at the $0 \iff -1$ transition can be seen in E) showing a good overlap of Rabi oscillations, which illustrate that a favorable polarization, in this case right circular polarization for the $0 \iff -1$ transition) needs 0.07 times less power to attain the same Rabi as compared with the less efficient circular polarization direction.

to root mean square (H_{RMS}) fields of 22.3 and 22.6 A m^{-1} and per watt (total input power) for the circular and linear modes respectively, and are in good agreement with the 22.8 A m^{-1} predicted by the simulations.

3.6. Experimental Characterization of Ellipticity

The peaks corresponding to the $0 \iff -1$ or the $0 \iff 1$ transitions can be modulated with the polarization of the MW signal. In particular, we can attenuate a given transition by appropriately choosing the direction of the circularly polarized MW signal, as can be seen in **Figure** 11A. This selective attenuation of peaks visualizes the capacity to independently modulate the efficiency of the two transitions by means of the direction of the circular polarization. Moreover, in Figure 11B we also observe that this selective control can be done also at different frequencies, demonstrating the verstality of the antenna. As can be observed from these figures, the attenuation is not complete, due to the geometrical orientation of the NV axis with respect to the antenna.

In order to show this, we have performed a more quantitative analysis. Figure 11C shows the Rabi oscillations on the $0 \iff -1$ transition for the two circularly polarizations with 1 W of power. It is observed that the oscillations become much slower when using the left circular polarization, as expected. The frequency of oscillation for left circular (green line) MW fields is about 3.7 times slower than when using the favorable right circular polarization (blue line). This can be visually seen in the figure, when comparing the oscillations of 0.07W power of right circular polarization with the 1W of left circular, as they overlap. As the frequency scales with the square root of the power, the rations of powers correspond very well with the expected values: $1/3.7^2 = 0.07$.

These values also agree with the expected behaviour given the orientation of the NV axis with respect to the antenna. The effective MW field inducing a transition is defined by the MW field orthogonal to the NV axis. For quantification purposes, this transition efficiency is often defined as a ratio between both circular polarization directions.[30] When the microwave field is perfectly circularly polarized and the NV axis is tilted by an angle *beta* with respect to the normal direction of the polarization plane (which lies on the plane of the antenna), the ratio of excitation from state $|0\rangle$ to state $|1\rangle$ with the two polarizations, will be $R = \frac{\Omega_{\text{clockwise}}}{\Omega_{\text{anti-clockwise}}} = \frac{1+\sin(\beta)}{1-\sin(\beta)}$. Given the [100] crystal configuration in our setup, all 4 NV axis orientations are at the same angle to the plane of the antenna, being $\alpha = 54,7°$ and $R = 3.7$, which is the one observed in our measurements (see Supporting Information for more details on the derivation of this ratio).

The same ration has been measured for two different excitation frequencies (see Figure 11A,B). This suggests that the polarization modulation is resilient to driving the antenna off-resonance as predicted in Figure 5. On the other hand, the measurements where performed at the center of the antenna, where we expect a minimal deviation from the circular polarization. As a qualitative measurement of the polarization inhomogeneities of the field produced by the antenna, we can use deviations from this optimal ratio.[30] Therefore, for a given circular polarization we set out to measure the contrast between the Rabi frequencies created by the $\langle 0| - 1\rangle$ and $\langle 0|1\rangle$ transitions. Given that the highest contrast is given for circular polarization, such that $\Omega_{\langle 0|-1\rangle}/\Omega_{\langle 0|1\rangle} = 3.7$, in **Figure** 12 we plot the results of measuring the divergence: $3.7 - \frac{\Omega_{\langle 0|-1\rangle}}{\Omega_{\langle 0|1\rangle}}$. Figure 12 was generated from two spacial Rabi maps with clockwise circularly polarised MW at 2.83 GHz ($0 \iff -1$) and 2.91 GHz ($0 \iff 1$), which correspond to the resonant transition frequencies for all 4 NV axis directions for an external magnetic field of 6 mT orthogonal to the

© 2024 The Author(s). Advanced Quantum Technologies published by Wiley-VCH GmbH

25119044, 2025, 3, Downloaded from https://advanced.onlinelibrary.wiley.com/doi/10.1002/qute.202400142 by Universidad del Pais Vasco Biblioteca Universitaria, Wiley Online Library on [02/04/2025]. See the Terms and Conditions (https://onlinelibrary.wiley.com/terms-and-conditions) on Wiley Online Library for rules of use; OA articles are governed by the applicable Creative Commons License

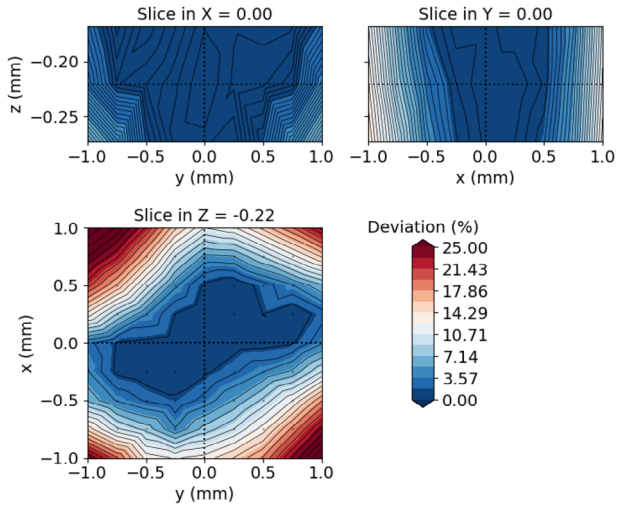

Figure 12. Measured spatial distribution of the ellipticity showing the difference between the measured Rabi maps at $m_s = 0 \Longleftrightarrow -1$ and the $m_s = 0 \Longleftrightarrow 1$ transitions correspondingly.

MW antenna (See Figure 11A,B). The field maps used to estimate Figure 12 can be found in the Supporting Information. The divergence from this ratio in the diamond suggest that the circularity is homogeneous over a large volume in the center and diverges towards the edges.

3.7. Power Test and Temperature Dependence

Increasing the power delivered in the center by feeding more power could cause damage to the antenna due to heating. To test this, the heat distribution is measured with an infrared thermometer. **Figure** 13C shows that the antenna can handle the maximum output power of the amplifier used, which is limited to 8W after transmission line losses. This temperature is below the safe human handling limits set for consumer electronics devices.[31] The antenna also shows a linear behaviour with the square root of the power as can be seen in Figure 13A.

Besides, it has been observed that the temperature increase generated a frequency shift in the resonant behaviour of the antenna. Figure 8B shows that the resonant frequency decreased by 16 MHz when increasing the temperature of the antenna from 22° *C* to 40° *C*.

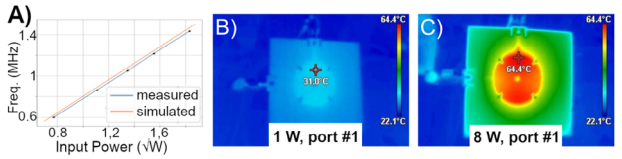

Figure 13. Power handling capability. A) Measured dependence of the Rabi frequency to the total input MW power for linearly polarized configuration. The Rabi frequency increases proportionally to the square root of the power, validating the linear behaviour of the MW antenna. The heat distribution in the antenna when put under 1 (B) and 8 (C) watts of continuous wave MW power on a single port.

4. Discussion

Our experience shows that, while the new geometry is effective, the built antennas tend to have a lower resonant frequency than predicted by simulations. We distinguish three possible factors: the dielectric constant might differ, fabrication inaccuracies might be present or spurious electrical capacitances that were not considered might exist. The shift is about 55 MHz in the manufactured prototypes, but this may vary from producer to producer. Given this tendency to shift, and the limitation that capacitor based tuning can only lower the resonance frequency, the authors recommend scaling down the outer diameter of the copper patch aiming for a higher resonant frequency than the desired one.

The results presented herein question the need to add 2 additional dummy ports (a total of 4 ports) to the PCB to achieve high homogeneity volumes by geometric symmetry, as found earlier.[25] Arguably, the addition of the two extra ports may reduce efficiency due to power leaking, which may partially justify that the design proposed here doubles the power efficiency as compared with the work of Herrmann et al.[25]. Note that they made the diamond hole size smaller and covered the ground plane hole with a copper socket, modifications which should have significantly increased the field strength.

The *H* field remains within 3 dB amplitude over almost 200 MHz, which is significantly higher than previously reported designs. However, the mentioned previous works estimated the BW from the reflection coefficient, which is a widespread practice based on the misleading assumption that the field generated in the antenna is proportional to the square root of the power not reflected. Figure 5A shows that using the S-parameter for this estimation is not precise, introducing a severe BW underestimation of 30% in our design. Accurate knowledge of the frequency response of the H-field is important to apply pre-emphasis and induce a flat field profile that enables precise spin control over a large range of frequencies.

Selecting another material with a higher dielectric constant could enable the attainment of higher magnetic fields and quality factors, as demonstrated in ref. [26]. It should be noted that materials with higher dielectric constants come at higher cost and are less available. Furthermore, although these materials can in principle enhance the performance, the antenna also becomes more susceptible to manufacturing and material imperfections.

The central hole in the antenna offers flexibility for adjustment of the diamond along the axis of the hole. For example, the diamond can be located at the height of the ground plane for applications benefiting from microscope objectives with short (>0.6 mm) working distances. However, the highest field strength versus homogeneity is achieved when the diamond is centered along the hole axis. In this configuration, the field inhomogeneity is below 7% within a volume of 1mm^3. This makes our configuration particularly suited to both harvest the averaging power of large pools of NV centers as well as those at moderate Rabi frequencies (>5 MHz), such as in dynamic nuclear hyperpolarization (DNP) and microfluidic NMR applications.

Importantly, the low inhomogeneity and ellipticity volumes largely overlap and cover the full 0.5 mm height of standard commercially available diamonds. Furthermore, this geometry enables matching seamlessly the volume geometry addressed with

© 2024 The Author(s). Advanced Quantum Technologies published by Wiley-VCH GmbH

25119044, 2025, 3, Downloaded from https://advanced.onlinelibrary.wiley.com/doi/10.1002/qute.202400142 by Universidad del Pais Vasco Biblioteca Universitaria, Wiley Online Library on [02/04/2025]. See the Terms and Conditions (https://onlinelibrary.wiley.com/terms-and-conditions) on Wiley Online Library for rules of use; OA articles are governed by the applicable Creative Commons License

the green pump beam. On the one hand, our configuration improves largely the coherence in the response of the large pool of NVs, which is paramount for bulk sensing in applications such as magnetometry with bulk diamonds. On the other hand, the large volume with low ellipticity and the on-demand shaping of the MW polarization allows polarization-dependent protocols over large NV ensembles. The fact that the Rabi frequency attenuation ratio between clockwise and counter-clockwise MW polarization remains at 3.7 for all different configurations shown in Figure 11 suggest that the ellipticity is low for a wide range of frequencies beyond the resonant frequency of the antenna, as predicted in Figure 5B. Note that the experimental ellipticity maps should not be taken as a direct measurement of the ellicticity because, as described in the Supporting Information, the effect on the Rabi is defined not only by the magnitude of the ellipticity but also by the orientation of the ellipticity with respect to each NV axis orientation. This explains that Figure 7 is geometrically different from Figure 12. Nonetheless, although this map should not be deemed as quantitative, it is useful to infer that the ellipticity is minimal over a large volume in the center of the diamond as predicted via the simulation.

The inhomogeneity and ellipticity of the antenna are almost not altered when it is driven off-resonance. This robustness together with the above-mentioned wide BW make this design very user-friendly, as it can offer high performance without the need for complex and time consuming tuning steps. Importantly, the regions with low inhomogeneity and those with low ellipticity overlap largely. Such high coherence over a large volume can enable high signal-to-noise ratios and high spin transition selectivity.

The ∼2 ns ringing time of the antenna does not impose a hazardous limitation as it is very short compared to those required for popular π and $\pi/2$ pulses, which are more than an order of magnitude longer for the Rabi frequencies generated by this antenna. For example, achieving a $\pi/2$ pulse in 50 ns would require <20 W input power in the circularly polarized mode, which is enabled by the good linearity (Figure 13A). The power can be safely increased to a maximum of 8 W in the continuous-wave mode without additional cooling (see Figure 13A,B). The structure could tolerate higher powers in pulsed mode to increase the MW field strength even further. Such higher powers could be implemented by using a pair of power amplifiers like the one used in this work to drive each port in this work. This feature would also facilitate fine-tuning each port's phase and amplitude to minimize the ellipticity in the induced MW field.

The direction of the circular polarization could be dynamically switched or adjusted, for example, by driving independently each port with a two channel arbitrary waveform generator or, for lower budget setups, by swapping the order of the transmission paths with fast switches. It is important to note the ellipticity of the field maps for linear polarization feeds. This ellipticity introduces a linear polarization component that limits the degree of isolation achievable when trying to address the –1 and +1 spin states independently.

5. Conclusion

Our results show that our antenna design offers a good compromise compared with other antennas used in NV centers measurements. Our design doubles the power efficiency, offers improved optical access and, most importantly, is robust against the variability of external hardware components, in contradiction to the previous patch antenna.[25] By an inhomogeneity of 14% in a 1 mm^3 volume, the proposed resonant MW antenna can address large ensembles of NVs in bulk diamond. Furthermore, this volume of low inhomogeneity can be easily and efficiently addressed optically. This limits the signal acquisition to only the NV centers that are coherently driven, which is paramount in boosting sensing precision. Additionally, a large part of the low inhomogeneity volume also shows low ellipticity. Our antenna design is particularly appealing for sensing experiments that benefit from lifting the –1 and +1 spin degeneracy without forcing an external magnetic field, such as at natural earth field conditions or at zero field. Importantly, unlike preceding works, we have analyzed the antenna's inhomogeneity and ellipticity in off-resonance driving conditions, validating the reliability of the design in practical working conditions. The H-field strength is also high over a large BW, and we show that this frequency response should not be estimated indirectly from the S-parameters but from more direct methods. The antenna's versatility is enhanced by its capability to become broadband over a wide range of frequencies through capacitors or varactors. Its homogeneity also allows for easy positioning and repositioning without sacrificing accuracy on the flip angle.

There is no MW antenna commercially available that is tailored to NV applications, each lab needing to craft its own. The proposed antenna is inexpensive and easy to reproduce as we share the files to manufacture it on standard double-sided PCB. Thereby, given its performance, versatility and robustness, this antenna can be a go-to solution for a wide range of high-end NV based quantum technologies in many labs.

Supporting Information

Supporting Information is available from the Wiley Online Library or from the author.

Acknowledgements

This project was supported in part by European Union's Marie Skłodowska-Curie project nr. 101030868, Erasmus+ exchange program from the European Union, the project I+D+i LINEAS ESTRATÉGICAS PLEC2021 from the Spanish Government (European NextGeneration funds), the Basque Government through the ELKARTEK 2022 program under Grant KK-2022/00062, the Programa Gipuzkoa Quantum 2023 - QUAN-000027-01 grant from the Diputación Foral De Gipuzkoa and the Plataforma de Tecnologías Cuánticas PTI-01 from CSIC. R.P.G. acknowledges the Ramón y Cajal (RYC2023-044021-I) research fellowship. J.C. acknowledges the Ramón y Cajal (RYC2018-025197-I) research fellowship, the financial support from Spanish Government via the Nanoscale NMR and complex systems (PID2021-126694NB-C21) project, and the Basque Government grant IT1470-22.

Conflict of Interest

The authors declare no conflict of interest.

© 2024 The Author(s). Advanced Quantum Technologies published by Wiley-VCH GmbH

25119044, 2025, 3, Downloaded from https://advanced.onlinelibrary.wiley.com/doi/10.1002/qute.202400142 by Universidad del Pais Vasco Biblioteca Universitaria, Wiley Online Library on [02/04/2025]. See the Terms and Conditions (https://onlinelibrary.wiley.com/terms-and-conditions) on Wiley Online Library for rules of use; OA articles are governed by the applicable Creative Commons License

Data Availability Statement

The data that support the findings of this study are openly available in qnanolab/MW_patch_Antenna_NVs: First formal release at https://doi.org/10.5281/zenodo.10529652, reference number 10529652.

Keywords

diamonds, microwave antenna, nitrogen vacancy centere, open-source, quantum sensing

Received: March 30, 2024
Revised: October 22, 2024
Published online: November 29, 2024

[1] R. Schirhagl, K. Chang, M. Loretz, C. L. Degen, *Annu. Rev. Phys. Chem.* **2014**, *65*, 83.
[2] R. Budakian, A. Finkler, A. Eichler, M. Poggio, C. L. Degen, S. Tabatabaei, I. Lee, P. C. Hammel, E. S. Polzik, T. H. Taminiau, R. L. Walsworth, P. London, A. B. Jayich, A. Ajoy, A. Pillai, J. Wrachtrup, F. Jelezko, Y. Bae, A. J. Heinrich, C. R. Ast, P. Bertet, P. Cappellaro, C. Bonato, Y. Altmann, E. Gauger, *arXiv preprint arXiv:2312.08841* **2023**.
[3] C. L. Degen, F. Reinhard, P. Cappellaro, *Rev. Mod. Phys.* **2016**, *89*, 3.
[4] M. W. Doherty, N. B. Manson, P. Delaney, F. Jelezko, J. Wrachtrup, L. C. Hollenberg, *Phys. Rep.* **2013**, *528*, 1.
[5] V. M. Acosta, A. Jarmola, E. Bauch, D. Budker, *Phys. Rev. B: Condens. Matter Mater. Phys.* **2010**, *82*, 20.
[6] Á Gali, *Nanophotonics* **2019**.
[7] T. Lenz, A. Wickenbrock, F. Jelezko, G. Balasubramanian, D. Budker, *Quantum Sci. Technol.* **2021**, *6*, 034006.
[8] P. J. Vetter, A. Marshall, G. T. Genov, T. F. Weiss, N. Striegler, E. F. Großmann, S. Oviedo-Casado, J. Cerrillo, J. Prior, P. Neumann, F. Jelezko, *Phys. Rev. Appl.* **2022**, *17*, 4.
[9] T. P. Alegre, C. Santori, G. Medeiros-Ribeiro, R. G. Beausoleil, *Phy. Rev. B: Condens. Matter Mater. Phys.* **2007**, *76*, 16.
[10] J. M. Schloss, J. F. Barry, M. J. Turner, R. L. Walsworth, *Phys. Rev. Appl.* **2018**, *10*, 034044.
[11] D. Le Sage, K. Arai, D. R. Glenn, S. J. DeVience, L. M. Pham, L. Rahn-Lee, M. D. Lukin, A. Yacoby, A. Komeili, R. L. Walsworth, *Nature* **2013**, *496*, 486.
[12] J. M. Taylor, P. Cappellaro, L. Childress, L. Jiang, D. Budker, P. R. Hemmer, A. Yacoby, R. Walsworth, M. D. Lukin, *Nat. Phys.* **2008**, *4*, 810.
[13] D. R. Glenn, D. B. Bucher, J. Lee, M. D. Lukin, H. Park, R. L. Walsworth, *Nature* **2018**, *555*, 351.
[14] E. Abe, K. Sasaki, *J. Appl. Phys.* **2018**, *123*, 161101.
[15] D. B. Bucher, D. P. Aude Craik, M. P. Backlund, M. J. Turner, O. Ben Dor, D. R. Glenn, R. L. Walsworth, *Nat. Protoc.* **2019**, *14*, 2707.
[16] Y. Wang, Y. Liu, H. Guo, X. Han, A. Cai, S. Li, P. Zhao, J. Liu, *Appl. Phys. Express* **2020**, *13*, 112002.
[17] O. R. Opaluch, N. Oshnik, R. Nelz, E. Neu, *Nanomaterials* **2021**, *11*, 8.
[18] K. Sasaki, Y. Monnai, S. Saijo, R. Fujita, H. Watanabe, J. Ishi-Hayase, K. M. Itoh, E. Abe, *Rev. Sci. Instrum.* **2016**, *87*, 053904.
[19] K. Bayat, J. Choy, M. Farrokh Baroughi, S. Meesala, M. Loncar, *Nano Lett.* **2014**, *14*, 1208.
[20] Y. Chen, H. Guo, W. Li, D. Wu, Q. Zhu, B. Zhao, L. Wang, Y. Zhang, R. Zhao, W. Liu, F. Du, J. Tang, J. Liu, *Appl. Phys. Express* **2018**, *11*, 12.
[21] P. London, P. Balasubramanian, B. Naydenov, L. P. McGuinness, F. Jelezko, *Phys. Rev. A: At., Mol., Opt. Phys.* **2014**, *90*, 1.
[22] M. Mrózek, J. Mlynarczyk, D. S. Rudnicki, W. Gawlik, *Appl. Phys. Lett.* **2015**, *107*, 1.
[23] T. P. Mayer Alegre, A. C. Torrezan, G. Medeiros-Ribeiro, *Appl. Phys. Lett.* **2007**, *91*, 20.
[24] R. Staacke, R. John, M. Kneiß, C. Osterkamp, S. Diziain, F. Jelezko, M. Grundmann, J. Meijer, *J. Appl. Phys.* **2020**, *128*, 19.
[25] J. Herrmann, M. A. Appleton, K. Sasaki, Y. Monnai, T. Teraji, K. M. Itoh, E. Abe, *Appl. Phys. Lett.* **2016**, *109*, 183111.
[26] V. Yaroshenko, V. Soshenko, V. Vorobyov, S. Bolshedvorskii, E. Nenasheva, I. Kotel'nikov, A. Akimov, P. Kapitanova, *Rev. Sci. Instrum.* **2020**, *91*, 3.
[27] Open source PCB repository, https://doi.org/10.5281/zenodo.10529652, Accessed: 2024-01-18.
[28] C. A. Balanis, *Antenna Theory: Analysis and Design*, Wiley, **2016**.
[29] M. Zhang, N. Llaser, in *2020 27th IEEE International Conference on Electronics, Circuits and Systems (ICECS)*, **2020**, pp. 1–4.
[30] M. Li, N. Zhang, L. Xu, J. Zhang, G. Bian, P. Fan, S. Wang, H. Yuan, *Phys. Rev. Appl.* **2023**, *19*, 054088.
[31] International Electrotechnical Commission (IEC), Audio/video, information and communication technology equipment - Part 1: Safety requirements, **2023**.

© 2024 The Author(s). Advanced Quantum Technologies published by Wiley-VCH GmbH

25119044, 2025, 3, Downloaded from https://advanced.onlinelibrary.wiley.com/doi/10.1002/qute.202400142 by Universidad del Pais Vasco Biblioteca Universitaria, Wiley Online Library on [02/04/2025]. See the Terms and Conditions (https://onlinelibrary.wiley.com/terms-and-conditions) on Wiley Online Library for rules of use; OA articles are governed by the applicable Creative Commons License